Title

Renal Arterial Network Structure by Computed Tomography, and Nephron-Arterial Interactions

Authors

Postnov, Dmitry
Holstein-Rathlou, Niels-Henrik
Sosnovtseva, Olga
et al.

Publication Date

2015

Peer reviewed

Am J Physiol Renal Physiol 313: F351–F360, 2017.
First published April 19, 2017; doi:10.1152/ajprenal.00092.2017.

RESEARCH ARTICLE

Architecture of the rat nephron-arterial network: analysis with micro-computed tomography

Donald J. Marsh,[1] Dmitry D. Postnov,[2] Douglas J. Rowland,[3] Anthony S. Wexler,[4] Olga V. Sosnovtseva,[2] and Niels-Henrik Holstein-Rathlou[2]

[1]*Department of Molecular Pharmacology, Physiology, and Biotechnology, Brown University, Providence, Rhode Island;* [2]*Department of Biomedical Sciences, Panum Institute, University of Copenhagen, Copenhagen, Denmark;* [3]*Department of Biomedical Engineering and Center for Molecular and Genomic Imaging, University of California, Davis, Davis, California; and* [4]*Department of Mechanical and Aerospace Engineering, University of California, Davis, Davis, California*

Submitted 21 February 2017; accepted in final form 13 April 2017

Marsh DJ, Postnov DD, Rowland DJ, Wexler AS, Sosnovtseva OV, Holstein-Rathlou N. Architecture of the rat nephron-arterial network: analysis with micro-computed tomography. *Am J Physiol Renal Physiol* 313: F351–F360, 2017. First published April 19, 2017; doi:10.1152/ajprenal.00092.2017.—Among solid organs, the kidney's vascular network stands out, because each nephron has two distinct capillary structures in series and because tubuloglomerular feedback, one of the mechanisms responsible for blood flow autoregulation, is specific to renal tubules. Tubuloglomerular feedback and the myogenic mechanism, acting jointly, autoregulate single-nephron blood flow. Each generates a self-sustained periodic oscillation and an oscillating electrical signal that propagates upstream along arterioles. Similar electrical signals from other nephrons interact, allowing nephron synchronization. Experimental measurements show synchronization over fields of a few nephrons; simulations based on a simplified network structure that could obscure complex interactions predict more widespread synchronization. To permit more realistic simulations, we made a cast of blood vessels in a rat kidney, performed micro-computed tomography at 2.5-μm resolution, and recorded three-dimensional coordinates of arteries, afferent arterioles, and glomeruli. Nonterminal branches of arcuate arteries form treelike structures requiring two to six bifurcations to reach terminal branches at the tree tops. Terminal arterial structures were either paired branches at the tops of the arterial trees, from which 52.6% of all afferent arterioles originated, or unpaired arteries not at the tree tops, yielding the other 22.9%; the other 24.5% originated directly from nonterminal arteries. Afferent arterioles near the corticomedullary boundary were longer than those farther away, suggesting that juxtamedullary nephrons have longer afferent arterioles. The distance separating origins of pairs of afferent arterioles varied randomly. The results suggest an irregular-network tree structure with vascular nodes, where arteriolar activity and local blood pressure interact.

renal vascular network; renal blood flow regulation; afferent arteriole distribution; nephron dynamics; network dynamics

TO REACH GLOMERULI, blood must flow through a network of arteries and arterioles. Here we analyze the network's structure. An ensemble of two mechanisms, tubuloglomerular feedback (TGF) sensing tubular fluid flow and the myogenic mechanism responding to a transmural hydrostatic pressure difference in afferent arterioles combine their actions in each nephron to regulate blood flow. Each mechanism independently generates self-sustained periodic oscillations, the oscillations synchronize, and the interaction enables TGF to modulate the amplitude and frequency of the myogenic oscillation (31, 33).

The TGF-myogenic ensemble acts by changing ionic permeabilities of smooth muscle cells, altering the cell membrane potential and propagating an electrical signal upstream along the vascular wall (34). Time-dependent changes in electrical potential serve as messages exchanged by nephrons through the vascular network, interactions that enable synchronization of blood flow oscillations among those nephrons (15, 19, 32, 46, 48, 49). Using a simulation of the renal vascular network, we predicted that minor changes in tubular length, by altering the transmission delay of the TGF signal to the macula densa, affected the pattern of synchronization on the network (35). Synchronization remained strong between near-neighbor nephrons and weakened with increased separation along the arterial tree. The oscillations in afferent arteriole diameter impose similar dynamics on blood flow and, therefore, on blood pressure in neighboring arteries. These pressure changes are virtually instantaneous, but the TGF oscillations involve transit delays, and phase angle differences between them reflect an interaction that disrupts synchronization.

Simulations of the synchronization pattern have been limited to nephrons with minor length variations and an idealized arterial structure (35). This simplified formulation suffers from two obvious problems: *1*) nephrons with long loops of Henle are longer than cortical nephrons and longer than those used in the simulation, and *2*) the range of their lengths is much greater. The idealized structure is just a first approximation. Preliminary simulation results with a mixture of different nephron lengths typical of cortical and juxtamedullary nephrons suggest increased complexity of the oscillations and show patterns not found in measurements from rats with normal blood pressure.

Experimental measurements of renal blood flow dynamics have been made from surface nephrons or from whole kidneys. Arterial network structures that differ from the ideal model could have a variety of effects on renal dynamics, but the lack of experimental methods for use on nephrons and blood vessels in different regions will restrict work in the immediate future to

Address for reprint requests and other correspondence: D. J. Marsh, Dept. of Molecular Pharmacology, Physiology, and Biotechnology, Brown University, Box G-B3, 171 Meeting St., Providence, RI 02912 (e-mail: donald_marsh@brown.edu).

mathematical models. Quantitative measures of arterial segments, arterial branching patterns, and arteriolar origins needed for these simulations are not available, nor is there an architectural construct. We report the results of measures of arterial architecture obtained from micro-computed tomography (CT) on a cast of the renal vasculature. The goal is to provide quantitative measures and organization of vascular structure for use in simulations. The results reveal features of the architecture not previously described and more complex than the idealized version used in our earlier simulations (35, 43).

METHODS

Animal. A renal vascular cast was made using a male Sprague-Dawley rat (295 g body wt; Taconic, Lille Skensved, Denmark). The experimental protocol was approved by the Danish National Animal Experiments Inspectorate and conducted in accordance with guidelines of the American Physiological Society. The rat was fed standard rat chow and allowed access to tap water ad libitum.

Anesthesia was induced in a chamber containing 8% sevoflurane (Sevorane, Abbott Scandinavia, Solna, Sweden) in 65% nitrogen-35% oxygen. The rat was placed on a servo-controlled heating table to maintain body temperature of 37°C. A tracheostomy was performed, and the rat was connected to a mechanical animal ventilator (tidal volume 0.8 ml/100 g body wt) at a frequency of 60 breaths/min. A final sevoflurane concentration of 2–2.5% maintained anesthesia.

The left renal artery was cannulated, and the left renal vein was opened and allowed to drain onto the peritoneal surface. The blood vessels of the kidney were flushed with normal Ringer solution to clear them of blood and blood plasma. A freshly prepared mixture of Mercox, a methacrylate resin, and its polymerizing agent was delivered into the renal artery cannula until the renal surface and the effluent from the renal vein turned white, the color of the Mercox-polymerizing agent mixture. After 10 min to permit completion of the polymerization reaction, the kidney was removed and placed overnight in a 2 M KOH solution for corrosion removal of tissue. The cast was then rinsed with water and dried in air.

Image acquisition. The kidney cast was imaged at the Center for Molecular and Genomic Imaging (University of California, Davis) with X-ray CT. We glued the cast to a fiberglass rod oriented with the imaging cylinder perpendicular to the coronal plane of the kidney and mounted the rod in a pin-vice sample holder. X-ray tomographic images were obtained on the Center's MicroXCT-200 specimen CT scanner (Carl Zeiss X-ray Microscopy). The CT scanner has a variable X-ray source capable of a voltage range of 20–90 kV with 1–8 W of power. We obtained two scans at different voxel sizes, isotropic low and high resolution at 21.77 and 2.5 μm, respectively, resulting in a full field of view for the low-resolution scan. The high-resolution scan had a field of view with a cylinder diameter and height of 5 mm, allowing imaging from the pelvic space below the arcuate arteries to above the cast surface, a distance of ~4.5 mm. Scan parameters were adjusted on the basis of the manufacturer's recommended guidelines. First, the source and detector distances were adjusted on the basis of sample size and the optimal field of view for the given region of interest. No X-ray filtration was used. The optimal voltage and power settings were determined for optimal contrast; 40 kV and 200 μA were used for both scans. We obtained 1,600 and 2,400 projections (camera binning 2 and 1, respectively) over 360 degrees with 1 and 4 s per projection for the low- and high-resolution scans, respectively. The tomographic images were reconstructed with appropriate center shifts to provide artifact-free images. Beam hardening parameter values of 0.3 and 0.15 were used to minimize beam hardening artifacts. A smoothing filter of kernel size 0.7 was applied during reconstruction. Images were reconstructed into 16-bit values.

Image analysis. We used the Amira software package, version 5.6 (FEI, Hillsboro, OR), for analysis. The images generated by the tomography procedure form a stack orthogonal to the cylinder's axis (the *z*-axis). Images on the *xz*- and *yz*-planes are computed from the *z*-axis stack. Arteries and glomeruli were readily identified in the planar images. Afferent arterioles were identified as unbranched vessels connecting an artery with a glomerulus. We identified arteries and afferent arterioles, recorded the three-dimensional coordinates of their origins and insertions, and calculated their lengths. Coordinates of intermediate points were recorded when any of these vessels was curved, and the length was then calculated as the sum of the lengths of the individual chords. Coordinates of the center of glomeruli were also recorded. We outlined each structure using a Wacom tablet and stylus and reconstructed three-dimensional images of the objects. Each voxel in the three-dimensional sampling region was assigned a pointer to a segmented region, or it was left blank if not associated with a class of objects. These three-dimensional images were used as checks against duplicate voxel assignments and also to create the displays (see Figs. 3–6 and 9).

Capillaries, veins, and medullary vascular bundles were present in the images, but we made no measurements from them. For several reasons, we deliberately avoided measuring the diameters of any of the segmented structures. *1*) Perfusion of a kidney with anything other than blood causes it to swell, changing the pressure in and around all intrarenal structures. The magnitude of the changes cannot be calculated. *2*) The viscosities of both the Ringer solution and the resin differ from that of blood, so the axial pressure gradients in arteries and arterioles will differ from that in a blood-perfused organ. *3*) The viscosity of the resin increases as it undergoes polymerization, changing axial pressure gradients and reducing them to zero when flow stops completely. *4*) The diameters of some arteries change with axial distance as arterioles branch from them. *5*) Diameter data are used to calculate vascular resistance. Vascular resistance is inversely proportional to the fourth power of the diameter; small uncertainties in diameter lead to large uncertainties in resistance. The 2.5-μm resolution of the tomography process is not adequate to provide the arteriolar diameter values needed for such calculations.

Limiting sampling to a cylindrical region of arbitrary radius imposes an artificial boundary. Branches of the main renal artery in the rat follow a course parallel to the renal surface, branch into smaller arteries following a similar course, and also send branches toward the renal cortex to supply afferent arterioles. The arteries parallel to the renal surface neither begin nor end within the sampling cylinder; only the radius of the sampling cylinder determines their visible lengths. The branches originating from these surface-parallel arteries run, for the most part, toward the renal surface and are self-contained within the sampling region. Some of these higher-order branches and some afferent arterioles leave the region defined by the sampling cylinder and do not return; their numbers are cited in RESULTS but are not used in any of the statistical analyses. Within the cylinder, there are also glomeruli, the afferent arterioles of which originated from outside the cylinder; the numbers of glomeruli are also given in RESULTS. Three larger arteries, having already branched from surface-parallel arteries, entered the sampling region, branched farther within the sampling region, and gave origin to afferent arterioles. The source and branch order of these larger arteries were determined from low-resolution images, and data from them are included in RESULTS.

Statistical analysis. Results of various measures were aggregated by branch order. Because a number of measured variables were not normally distributed, we applied the Kruskal-Wallis test, a nonparametric single-factor analysis of variance by ranks, to determine whether average values differed from each other and, when indicated, Dunn's test to make multiple comparisons using rank sums (12). Significance of differences was assessed at $P = 0.05$.

RESULTS

Figure 1 shows low-resolution coronal, sagittal, and transverse sections of a CT image of the kidney cast. The high-

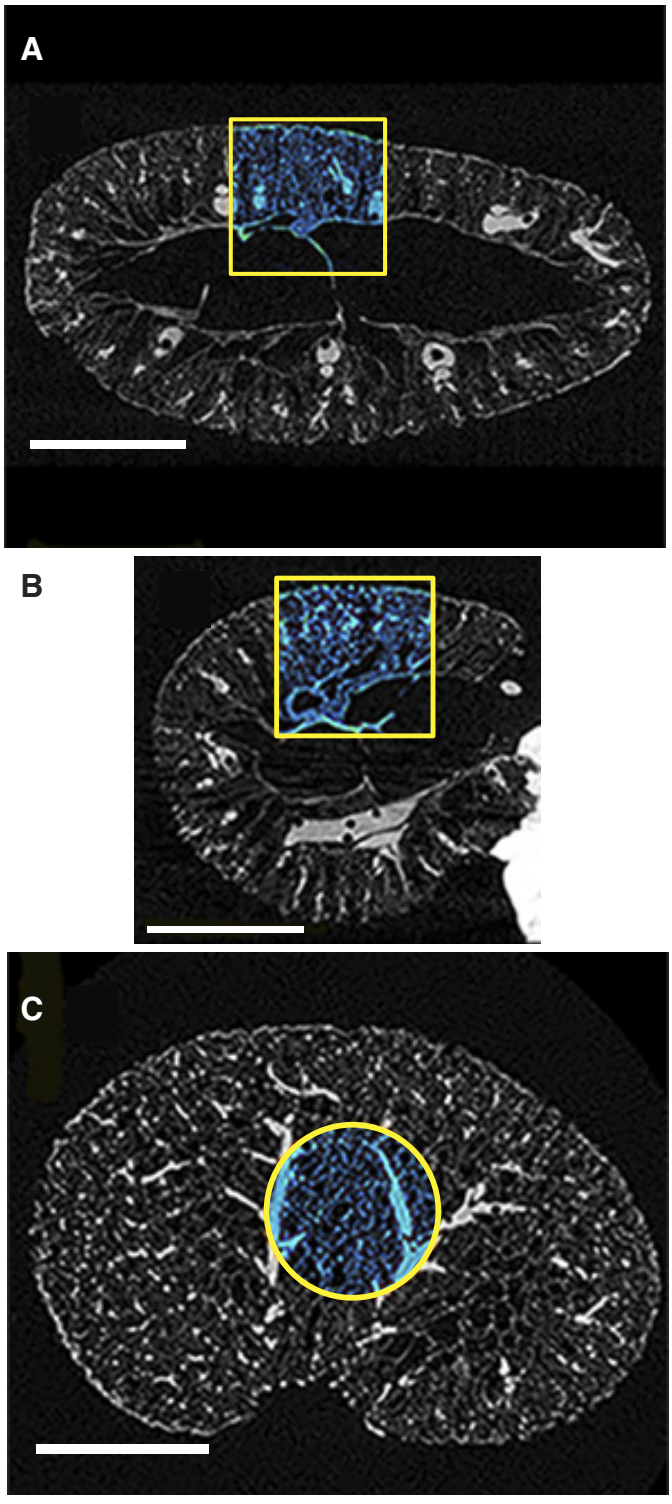

Fig. 1. Low-resolution (21.5-μm voxel edge) coronal (*A*), transverse (*B*), and sagittal (*C*) X-ray images of the renal cast. High-resolution (2.5-μm voxel edge) X-ray image is superimposed in blue. Cylindrical sampling window is outlined in yellow. Scale bar = 5 mm.

resolution images were made from the ventral surface in the area shown in blue and outlined in yellow. The sampling window extends from the renal pelvis to above the renal surface. We used the average *z*-coordinate value of the arcuate arteries as a reference point for the *z*-coordinate values of all other structures. The distance separating that reference point and the center of the glomerulus farthest from it along the *z*-axis was 2.12 mm.

Figure 2 presents high-resolution planar images showing the appearance of arteries, afferent arterioles, glomeruli, peritubular capillaries, and veins. Using images such as these, we measured three-dimensional coordinates at the origins and ends of arteries and afferent arterioles and at the centers of glomeruli.

Arteries. Figure 3 provides an oblique view of the arterial tree within the sampling cylinder. Arteries deepest in the renal parenchyma cross the sampling cylinder running approximately parallel to the renal surface; we designate these arcuate arteries (26). Branches originating from arcuate arteries turn toward the renal surface and undergo a series of branchings, with two, three, or four branch vessels originating from the distal end of each previous branch order. The number of these bifurcations needed to reach a terminal branch at the tree top varied from as few as two to as many as six.

Arterial branches of various orders either terminate in afferent arterioles or branch further. The order assignment of each vessel represents its place in a sequence of branches. We designate an artery terminal if its final bifurcation is into two or more arterioles. Two or more afferent arterioles that originate from the same location on an artery will develop stable synchronization, resistant to interference from different rhythms at more distant sites (35, 43). We posit that this stability will prove an important factor in the dynamics of the nephron-vascular network; therefore, we separate the results from terminal and nonterminal arteries to permit tests of this idea with mathematical models. In addition, the mathematical representation of the nephron-arterial network forms a multipoint boundary value problem, and the boundary conditions for terminal arteries will differ from those for nonterminal arteries.

We consider first the nonterminal arteries, the end branches of which comprise additional arteries. We will refer to this category of arteries as *motif 1*. We identified 113 such vessels distributed among the 6 branch orders. Seventeen other arteries left the sampling cylinder through its sidewalls, precluding length measurements. Figure 4 shows a first-order artery and a pair of second-order branches originating from it. The afferent arterioles originating directly from these nonterminal arterial segments and the glomerulus supplied by each afferent arteriole are also shown in Fig. 4.

Table 1 summarizes the results for nonterminal arteries, sorted by branch order number. The average length of all such arteries was 463.5 ± 255 (SD) μm, with no significant difference in length among the branch orders. Over all branch orders, the range of lengths was 109–1,314 μm. The arteries listed in Table 1 originate as branches of larger vessels and terminate at a branching point. The branches may form the next order of nonterminal arteries or end in a terminal artery. Table 1 shows the numbers of such branches for each order. The number of arteries increases in the first and second orders, reaches the largest number in the third order, and declines thereafter as each arterial tree reaches its terminal artery. Afferent arterioles originate directly from arteries of all branch orders (Figs. 2, 4, 5, and 6). The numbers of arterioles originating from each branch order are shown in Table 1.

We found two different patterns of terminal arteries: *1*) arterial pairs or triplets as the topmost branches of arterial trees

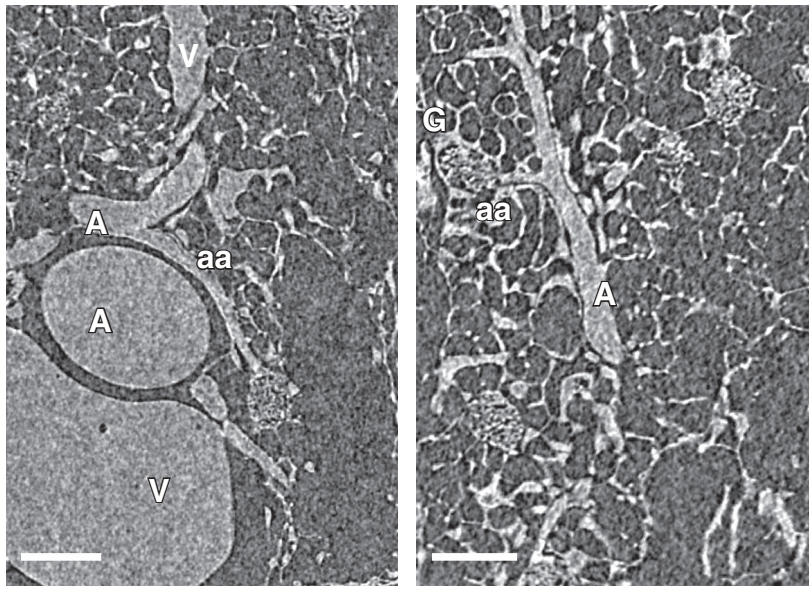

Fig. 2. High-resolution X-ray tomographic views of the cast showing arteries (A), veins (V), afferent arterioles (aa), and glomeruli (G). Scale bar = 200 μm.

and *2*) unpaired single vessels originating from arteries of different branch orders. The first of these terminal artery groups we designate *motif 2* (Fig. 5). The average length of all such terminal arteries was 378.3 ± 249 (SD) μm; the range of lengths was 45–1,075 μm. Afferent arterioles arose from all orders of these vessels.

Table 2 lists measurements made on terminal arteries of the topmost branches of the arterial trees. The number of these arteries within the sampling cylinder increased with order number, reaching a maximum at the fourth order and declining at higher orders as vascular trees reached their terminal ends. There were significant differences among these average lengths (Table 2). The two highest-order vessels were shorter than the lower-order vessels ($P < 0.05$). The average lengths of the lower-order arteries in this group did not differ significantly among themselves. Lower-order terminal branches originate farther from the renal surface than higher-order branches.

We also observed unpaired branches originating from nonterminal arteries, terminating in pairs of afferent arterioles, designated *motif 3*. Figure 6 illustrates the pattern and Table 3 shows measurements from this group. The number of these vessels increased with increasing branch order, reached its maximum at the fourth order, and declined at higher orders. There were no significant differences among the average lengths of the branch orders.

Arterioles and glomeruli. We recorded the coordinates of 1,196 afferent arteriole-glomerulus pairs. Of these, 24.5% originated directly from the nonterminal arteries of *motif 1*,

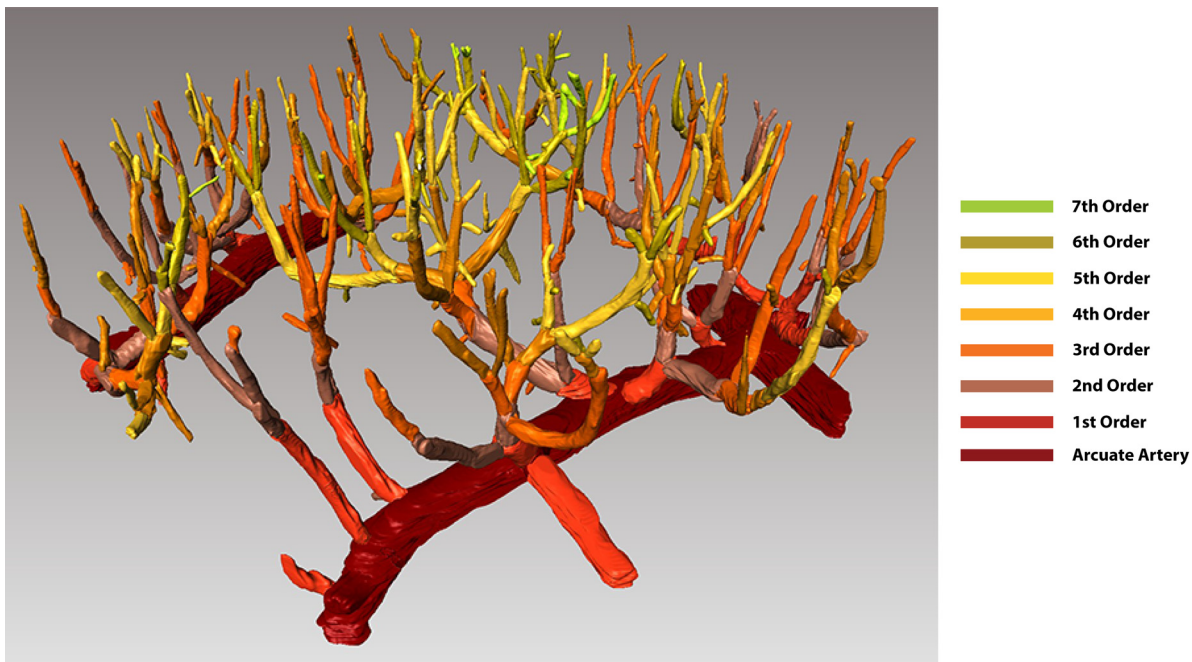

Fig. 3. Oblique 3-dimensional view of the reconstructed arterial network.

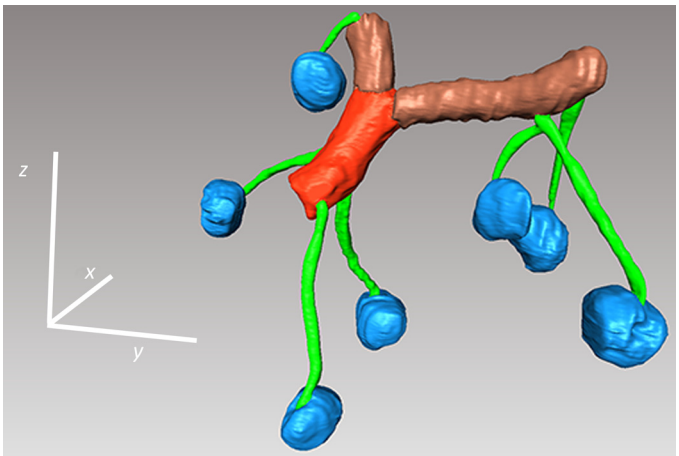

Fig. 4. A nonterminal artery and its bifurcation into a pair of nonterminal arteries, the afferent arterioles originating on the arteries, and the glomeruli supplied by the arterioles. The parent artery is a 358-μm-long 1st-order branch; its 2rd-order branches are 446 and 196 μm long. Color coding for the arteries as shown in Fig. 3. Afferent arterioles are green; glomeruli are blue.

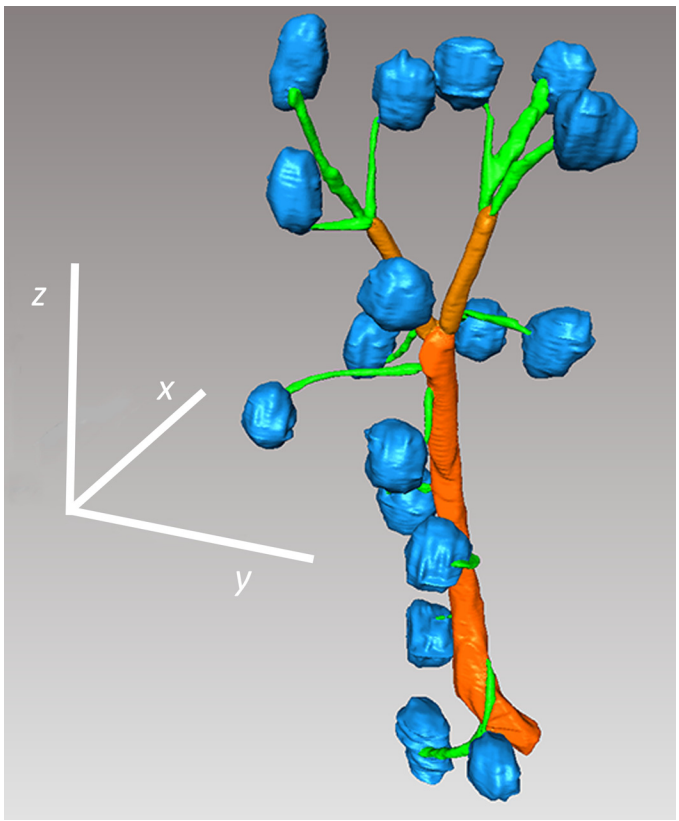

Fig. 5. A nonterminal artery and its bifurcation into a pair of terminal arteries at the top of their arterial tree, the afferent arterioles originating on and at the end of arteries, and the glomeruli supplied by the arterioles. The parent nonterminal artery is a 556-μm-long 3rd-order branch; the 4th-order terminal vessels are 206 and 79 μm long.

52.6% from terminal arteries of *motif 2* at the top of the arterial trees, and 22.9% from unpaired terminal arteries of *motif 3* originating from nonterminal arteries. The sampling cylinder contained another 74 glomeruli distributed within three glomerular diameters of the sampling cylinder's wall but not paired with afferent arterioles. We assume that the afferent arterioles supplying this group of glomeruli originated from arteries outside the sampling cylinder. Afferent arterioles could not be found for an additional 17 glomeruli that were not near the cylinder's wall.

We aggregated measurements of afferent arteriolar length in quartiles by distance along the *z*-axis (Table 4). The average length was greater in the quartile nearest the arcuate arteries than in the others; the difference was significant ($P < 0.001$). The other quartiles did not differ significantly among themselves ($P > 0.05$). Christensen et al. (11) found afferent arterioles and glomeruli of long-looped nephrons occupying the deepest regions of the cortex; the data in Table 4 complement the findings of Christensen et al., indicating that juxtamedullary nephrons have longer afferent arterioles than their cortical counterparts.

Table 1. *Length and branching of nonterminal arteries*

Branch Order No.	No. of Arteries	Avg Length, μm	No. of Branches			No. of Afferent Arterioles
			Pairs	Triplets	Quadruplets	
0						9
1	14	540 ± 268	10	4		39
2	29	553 ± 257	25	4		87
3	31	471 ± 260	23	6	2	72
4	22	351 ± 177	19	2	1	40
5	13	415 ± 307	12	1		31
6	4	262 ± 108	4			15

Arcuate arteries are listed as 0-order vessels. First-order branches originate from arcuate arteries, 2nd-order branches from 1st order, and so on. Number of arteries is a count within the sampling cylinder of the arteries of each order. Length of an arterial segment (mean ± SD) is measured as distance between the origin of a segment at one vascular node and its end at the next vascular node. Average arterial lengths were not significantly different from each other. Nonterminal arteries end at vascular nodes, where they branch into pairs, triplets, or quadruplets of arteries. Arterioles arise at different locations on the branch arteries. Counts of terminal branches at the tops of the arterial trees are included; measurements on terminal branches are included in Tables 2 and 3. Arteries leaving the sampling cylinder by crossing its wall are not included.

Figure 7 shows the cumulative distribution of glomeruli and afferent arteriolar origins along the *z*-axis. Negative distances mean that arteriolar origins or glomeruli originate deeper than the average depth of the arcuate arteries in the sampling region. Such cumulative distribution results occur when the data are from one of several distributions, including normal, lognormal, and logistic. This form of presentation shows whether the data set is from a uni- or a multivariate population. The results in Fig. 7 are typical of a univariate distribution. We interpret these results to mean that there are no local collections of glomeruli or afferent arterioles. The results in Table 4 differentiate afferent arterioles of juxtamedullary nephrons on the basis of their lengths and location near the corticomedullary junction. The results in Fig. 7 give no indication of further distinguishing geometry.

In a further effort to define organizational patterns, we measured the distance along the vasculature separating the origins of nearest-neighbor afferent arterioles. Except for the end-afferent arterioles of *motif 2* and *3* arteries, coordinates at the origin of each afferent arteriole were measured at the wall of its arterial segment. To avoid measuring a distance along an artery of uncertain diameter, we reduced the arterial segment to a center line connecting its ends and projected a perpendicular

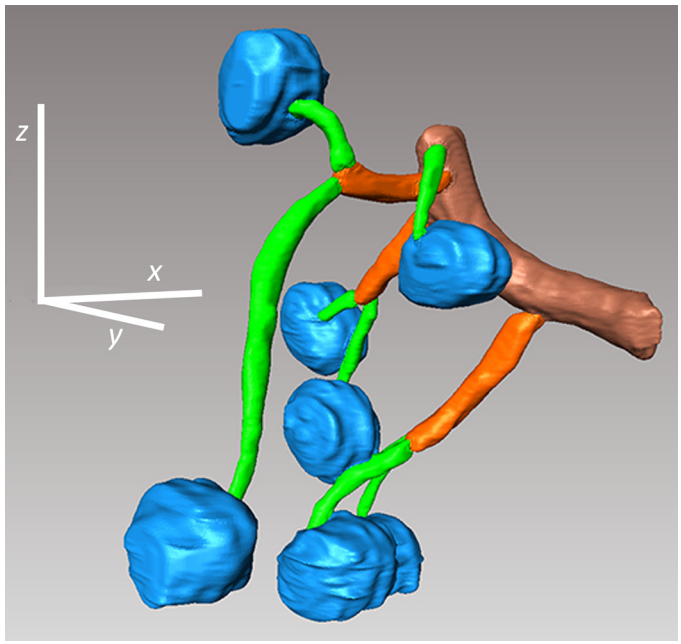

Fig. 6. A nonterminal artery and 3 unpaired terminal arteries, the afferent arterioles originating on and at the end of arteries, and the glomeruli supplied by the arterioles. The parent nonterminal artery is a 493-μm-long 2nd-order branch; its terminal branches are 185, 168, and 290 μm long.

from the afferent arteriole's origin point to the center line of the parent vessel.

Measuring these distances for all afferent arteriolar pairs required two different approaches. For the first group, we calculated the distance from the origin of each afferent arteriole to the closest afferent arteriole found upstream. Two or more arterioles originating from a common point were assigned a separation distance of 0 μm. We measured the distance separating 1,004 arteriolar pairs (Fig. 8*A*).

For the second group, we measured the distance between 661 nearest-neighbor afferent arterioles on arterial branches originating from a common branch point. Most of these pairs were arterioles on branches of a single parent artery; others included instances with no afferent arterioles on one of the branches. For the latter case, we tracked downstream from that branch until an afferent arteriole was found (Fig. 8*B*).

Table 2. *Length of terminal arteries at the top of the arterial tree and the number of afferent arterioles they form*

Branch Order No.	No. of Arteries	Avg Length, μm	No. of Afferent Arterioles	Afferent Arterioles/Artery
2	3	662 ± 195	24	8.0
3	25	517 ± 288	127	5.1
4	41	427 ± 250	176	4.3
5	37	352 ± 189	146	3.9
6	31	277 ± 203	125	4.0
7	10	168 ± 126	31	3.1

Each artery in this group originates as one of a pair, a triplet, or a quadruplet of branches and ends in a pair or a triplet of afferent arterioles. In addition to the afferent arterioles arising at the terminal end of these branches, other afferent arterioles arise at intermediate points. Dunn's procedure for multiple comparisons with rank sums (5) indicated that average lengths (means ± SD) of *orders 2, 3, 4*, and *5* did not differ significantly from each other, nor did the average lengths of *orders 6* and *7*.

Table 3. *Length of single terminal arteries not at the top of the arterial tree and the afferent arterioles they form*

Branch Order No.	No. of Arteries	Avg Length, μm	No. of Afferent Arterioles	Afferent Arterioles/Artery
1	1	432	2	2
2	3	144 ± 51	7	2.3
3	18	183 ± 110	48	2.7
4	36	158 ± 88	87	2.4
5	25	167 ± 111	71	2.8
6	15	178 ± 92	40	2.7
7	8	101 ± 45	19	2.4

Each artery in this group originates as a single vessel from various arterial branches, and not from vascular nodes. The terminal artery of *order 1* originated from an arcuate artery. Terminal arteries in this group often have afferent arterioles originating between the origin of the arterial branch and its end in addition to those at the end. One-way analysis of variance using the Kruskal-Wallis procedure indicated no significant differences among the average lengths (means ± SD) of branch *orders 2–7*.

The data for each group fit an exponential distribution, confirming our previous report (42). In the earlier study we used a different method to visualize the vasculature and had a smaller number of arterioles. As noted in that study, the finding of an exponential distribution differs from the lognormal distribution found in other organs (8, 44). Exponential distributions of these distances were found in all three motifs. An exponential distribution describes the distance (or the time) between events in a random (Poisson) process and indicates that the measured separations, in this case between afferent arteriolar origins, are independent of each other.

Figure 9, a view of the arterial network from above the renal surface, illustrates how arterial branches from adjacent arcuate arteries interdigitate; it shows the pathways linking the separate trees. An electrical signal, a composite of myogenic and TGF oscillations, originates from the afferent arteriole of each nephron and propagates along the vascular network. The interaction of nephrons, when it occurs, results from the interaction of these signals and causes synchronization of the nephron oscillations (31, 33, 45, 46). Surface nephrons, adjacent to each other but perfused by arterial trees arising from different arcuate arteries, would require an electrical signal from one to traverse both trees in order to reach the other. Interactions interfering with coherent signal communication lurk at every vascular node, reducing the probability of synchronization between arterial trees.

Table 4. *Lengths of afferent arterioles*

Quartile	Length, μm
1	232 ± 123
2	168 ± 75
3	172 ± 85
4	183 ± 80

Measured afferent arteriolar lengths (means ± SD) were grouped into quartiles by the location of their origins along the *z*-axis. Each quartile contained measurements from 299 arterioles. The 0 value on the *z*-axis was set at the average level of the arcuate arteries. According to the Kruskal-Wallis test, length values differed among themselves ($P < 0.001$). Dunn's test indicated that the average length of *quartile 1* differed from the average lengths of the other quartiles ($P < 0.001$) and that there was no difference among the average lengths of *quartiles 2, 3*, and *4* ($P > 0.05$).

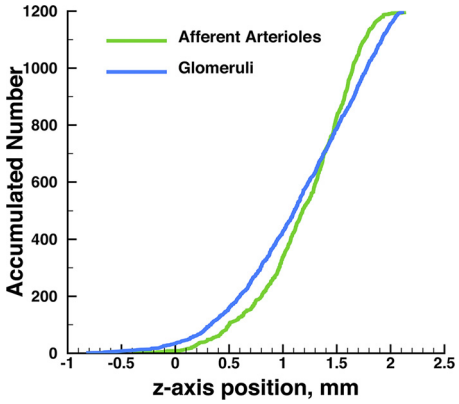

Fig. 7. Cumulative distributions of afferent arteriolar origins and glomeruli along the *z*-axis. Each curve consists of 1,196 points. The reference level is the average depth of the arcuate arteries. Structures lying deeper than arcuate arteries have negative distances.

DISCUSSION

We made a polymer cast of the vasculature in a single kidney of a normotensive adult male rat, subjected the cast to CT with 2.5-μm resolution, and recorded three-dimensional coordinates of arterial segments, afferent arterioles, and glomeruli. We designed the study to define organizational patterns in the preglomerular arterial and arteriolar network as an anatomic basis for mathematical models of network dynamics, to measure the length of each segment of each vessel type, and to test the length results for significant differences.

As noted in METHODS, the casting procedure induces a series of pressure and volume changes within the kidney. Interpretation of the results requires the assumption that structural integrity of intrarenal vascular objects survives the cast formation process, even though the exact dimensions may change, and that the forces causing the volume changes act isotropically. There was no evidence of extravasation of the casting material, either within the sampling window or elsewhere in the kidney. The casting material appeared within arteries, arterioles, glomeruli, peritubular capillaries, veins, and venules and also in vessels forming vascular bundles of the renal medulla. These observations show that the cast material filled the vascular space, preserving its structural continuity. As discussed in METHODS, we decided against measuring diameters of any vascular structure. The casting procedure generates unknowable pressure changes, with unpredictable effects on diameters, particularly in smaller vessels such as afferent arterioles, leaving us unable to guarantee the validity of any diameter measurement.

Arteries within the kidney form a demand-driven, load-balanced, globally connected resource distribution network. The resource is blood, single-nephron autoregulation provides the demand, interactions in the network support continuous perfusion of all nephrons, and the connection to the renal artery as a single network source provides the basis for interactions among all nephrons. Disparities between experimental results and network model predictions (see below) motivate this study.

The cast revealed an arterial tree network originating in arcuate arteries, branching as few as twice or as many as six times before reaching a terminal artery that terminated in pairs, triplets, or quadruplets of afferent arterioles. Afferent arterioles originated directly from all branch orders of nonterminal arteries (*motif 1*), from paired terminal arteries forming the tops of the arterial trees (*motif 2*), and from unpaired terminal arteries branching from all orders of nonterminal arteries (*motif 3*). The lengths of *motif 1* arteries did not vary with branch order, nor did those of *motif 3*. *Motif 2* arteries became significantly shorter when they originated from higher-order branches. Afferent arterioles originating from *motif 2* arteries supplied one-half of the glomeruli; arterioles arising from *motif 1* or *motif 3* arteries each supplied one-quarter of the glomeruli.

We aggregated the afferent arterioles into quartiles according to the *z*-axis location of their origins. The quartile closest to

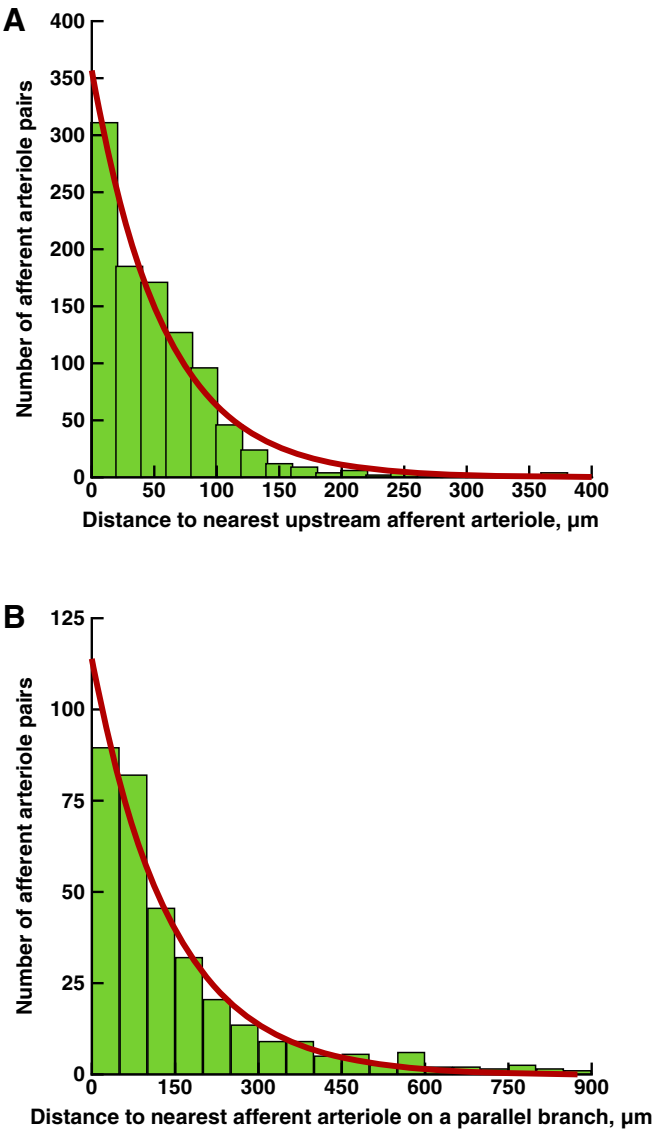

Fig. 8. Separation of afferent arteriolar origins. *A*: distribution of distance separating 2 nearest afferent arteriolar origins, from downstream to upstream. *B*: distribution of distance separating 2 nearest afferent arteriolar origins, from one branch vessel to another branch, designated parallel branches. Most of these pairs were arterioles on branches of a single parent artery; others included instances with no afferent arterioles on one of the branches. For the latter case, we tracked downstream from that branch until an afferent arteriole was found. Red lines are least-square exponential fits to the function $y = ae^{kx}$ to each data set: $a = 431.9$, $k = -0.017$, and adjusted $R^2 = 0.98$ (*A*) and $a = 114.7$, $k = -0.007$, and adjusted $R^2 = 0.97$ (*B*).

Fig. 9. Arterial tree shown in Fig. 3, viewed from above the surface of the cast and looking down the *z*-axis.

the renal medulla had significantly longer arterioles than the three others. Juxtaglomerular nephrons are thought to comprise one-quarter to one-third of the full nephron population. Christensen et al. (11) reported that juxtamedullary nephrons and their glomeruli are closer to the medulla than cortical nephrons; our results, therefore, suggest that afferent arterioles of juxtamedullary nephrons are longer than their counterparts in cortical nephrons.

We also measured the distances separating successive origins of afferent arterioles. An exponential distribution described these distances, in agreement with our previous results (42). All three motifs had similar exponential distributions. Exponential distributions arise from Poisson processes and describe random occurrences of differences in distance; each portion of the space has the same probability of containing an object, and the presence of an object in any portion of the space has no influence on the occurrence of another object in any portion of the space. In the specific instance of afferent arteriolar origins and the distance separating them, the space is the arterial network, the objects are the distances between arteriolar origins, and the finding of an exponential distribution implies that there is no mathematical function capable of predicting the location of any such pair of origins or the magnitude of the distance. Under such circumstances, probabilistic assignments provide a way to model the dynamics of blood flow regulation, a method we applied in our earlier study (42).

A number of investigators have measured different aspects of the renal arterial vasculature. More and Duff, who made neoprene casts on kidneys from human cadavers, were among the first (37). They measured afferent arteriolar lengths and reported results similar to those in Table 4. They also showed afferent arterioles arising directly from arteries of different branch orders, similar to those in Figs. 2 and 3–5. Casellas et al. dissected renal arterial trees in four mammalian species and found afferent arterioles originating from interlobular arteries, often in pairs, triplets, and quadruplets (7). They also measured lengths of afferent arteriole pairs and found that two arterioles forming a pair had similar lengths, a result they interpreted to provide a favorable basis for synchronization.

Beeuwkes (3) and Beeuwkes and Bonventre (4) made silicone rubber casts of dog kidney vasculature and injected tubules with micropipettes. They studied distribution patterns of efferent arteriolar outflows, a subject not addressed in our work. Horacek et al. (21, 22) made vascular casts of monkey kidneys and also found afferent arterioles originating directly from arteries in the renal cortex. Their findings were characterized qualitatively; no quantitative results were reported.

Kriz and Bankir published a summary of renal tubular and vascular anatomy and recommended a standard nomenclature (26). Their description of tubular anatomy was extensive; their description of vascular anatomy was less so. Their representation of the arterial vasculature showed a single vessel, originating from an arcuate artery and proceeding directly to the renal surface; afferent arterioles originated from various sites on this unbranched vessel. Our results provide a more detailed view, with a treelike branching structure and no unbranched vessels reaching the renal surface. They named the single vessel the cortical radial artery, but our results reveal no single structure to which that name could be applied.

Nordsletten et al. (39) provided the most detailed and quantitative description of the renal vasculature currently available. They worked with CT images prepared by Garcia-Sanz et al. (14) from a vascular cast of a rat kidney and used skeletonization, an image analysis method that traces the pathway of contiguous vessels, reducing each segment to a center line while retaining diameter data. They then applied Strahler ordering (47) to sort and interpret the data. Strahler ordering sorts treelike networks by the diameter of the branches according to a branching scheme and has been applied to coronary (25) and pulmonary (23) arteries. The principal assumption required for its use is the existence of a diameter-based hierarchy of vessels, ending in the narrowest vessels, i.e., afferent arterioles in the kidney. This assumption has not been tested in renal vessels. Marxen et al. (36) questioned the suitability of the Strahler order scheme for describing the renal vasculature. Strahler ordering led Nordsletten et al. to the conclusion that all afferent arterioles originated from terminal arteries at the top of the vascular tree. Afferent arterioles branching from larger arteries, as in the present study and earlier studies (6, 20–22, 37), contradict the assumption and the conclusion reached from its application. Postnov et al. (42) also found inconsistencies between the data reported by Nordsletten et al. (39) and Murray's law (38).

We selected a rat kidney imaged on its ventral surface for this project, because all the experimental data we intend to use for model validation were collected from the ventral surface of rat kidneys. The rat kidney has a single lobe, but other species, human, primate, dog, and rabbit, have kidneys with multiple lobes. We have not tested for species differences in the measurements we present, and that possibility remains.

We carried out this study to provide a quantitative basis for mathematical modeling of dynamics on the arterial nephron network, prompted by a discrepancy between experimental and simulation results. Measurements of tubular pressure (15, 17, 29, 49), efferent arteriolar blood flow (50), and nephron blood

flow (18) show the periodic oscillations attributable to TGF. The results, all collected from normotensive rats, appear consistently in surface cortical nephrons.

A computer simulation of a single nephron reproduced the results of measurements in single cortical nephrons (31). A multinephron model with 16 nephrons, configured with identical parameter sets and connected within an idealized arterial network, also predicted the tubular pressure oscillations (35). With nephron lengths made to vary randomly by 1–2%, the oscillations had frequencies similar to those generated by the single-nephron model, but not identical to each other, and with slower oscillations superimposed.

Oscillators synchronize when they interact if the natural frequencies are similar enough to permit them to entrain at a common frequency. The presence of synchronization signals an interaction. Synchronization of measured tubular pressure in rat nephrons occurred only in arterioles directly adjacent to each other originating from a single branch of an arterial tree (49). Laser speckle contrast microscopy of the renal surface showed synchronization in groups of two or three adjacent nephrons, but not more broadly (18). The model with a simplified arterial tree predicts greater synchronization than direct measurements show, but not a change in state. Elongation of 1 of the model's 16 nephrons to simulate a medullary nephron causes all nephrons to bifurcate to chaotic dynamics, no longer predicting periodic oscillations (unpublished results). Juxtamedullary nephrons operate continuously as part of the arterial-nephron network; the version of the multinephron model that includes a juxtamedullary nephron, therefore, fails to predict the nephron dynamics observed in experiments. Synchronization patterns in a complex network of oscillators depend on a pattern of interactions (40). The failure of a model to predict a measured pattern of synchronization suggests that the model might not adequately represent the interaction pattern.

Interactions of various elements in the arterial-nephron network lead to synchronization. For example, the combined action of TGF and the myogenic mechanism provides regulation of single-nephron blood flow. Each mechanism generates a self-sustained oscillation, and the oscillations synchronize, reflecting their interaction (10, 13, 31, 33, 46, 50). The interaction enables TGF, with its longer period, to modulate both the amplitude and frequency of the myogenic oscillation (31, 33). Modulation reduces the myogenic response to increased arterial blood pressure, ensuring that a signal reaches the macula densa to sustain a regulated flow into the distal nephron (50).

Additional interactions affect local blood flow within the arterial network. The time-varying electrical potential difference generated by the TGF-myogenic ensemble contains both oscillations and propagates retrograde toward the nearest vascular node (34). This propagated oscillating change in membrane potential functions as a signal, broadcasting information about the activity of its nephron source. Similar signals from other afferent arterioles reach the vascular node, and the interaction among them enables synchronization of oscillations from the participating nephrons (9, 15, 18, 34, 46). These synchronization events increase the stability of the oscillations (1, 2, 27, 28, 41) and augment the force of smooth muscle contraction in response to a signal from the macula densa (24). Mean arterial blood pressure in conscious animals fluctuates over time scales of minutes to hours in a 1/*f* pattern (16, 30). The larger fluctuations can exceed 20 mmHg. The increased force of contraction available because of nephron-nephron synchronization enhances the likelihood of an effective autoregulatory response to these fluctuations.

The periodic contraction imposed by the TGF-myogenic ensemble on afferent arterioles causes a periodic change in the vessel's vascular resistance, affecting upstream blood pressure. On the time scale defined by the periods of the TGF and myogenic oscillations, the change in upstream arterial pressure is rapid and propagates quickly to adjacent arterial branches and upstream nodes. The time required for a fluid wave to travel from glomerulus to macula densa determines the relatively slow reaction time of the TGF-myogenic ensemble. If several pairs of synchronized afferent arterioles, each with a different TGF frequency, converge to a single vascular node, synchronization with the node's arterial pressure may fail, interfering with synchronization among the nephron pair groups. This interaction could, therefore, interrupt synchronization and limit the size of synchronized nephron clusters. Theoretical networks with oscillating active elements can generate a variety of synchronization patterns, leading to distinct synchronized clusters, each operating at its own frequency (40).

This set of comparisons suggests to us that to be validated against experimental results a network model must reflect the level of structural complexity we measured in this study. Nephrons in various regions of the kidney have different functional roles requiring autonomous regulation of blood flow. At stake is an understanding of how the kidney sustains this functional differentiation.

GRANTS

The work of D. J. Marsh was supported by a grant from the Lundbeckfonden of Copenhagen, Denmark; D. D. Postnov, O. V. Sosnovtseva, and N.-H. Holstein-Rathlou by a grant from the University of Copenhagen to its Dynamical Systems Interdisciplinary Network; and A. S. Wexler by National Institute of Environmental Health Sciences, University of California, Davis Core Center Grant P30 ES-013513.

DISCLOSURES

No conflicts of interest, financial or otherwise, are declared by the authors.

AUTHOR CONTRIBUTIONS

D.J.M. and N.-H.H.-R. conceived and designed research; D.J.M., D.R., and N.-H.H.-R. performed experiments; D.J.M., D.D.P., and A.S.W. analyzed data; D.J.M., D.D.P., A.S.W., O.V.S., and N.-H.H.-R. interpreted results of experiments; D.J.M., D.D.P., and D.R. prepared figures; D.J.M. drafted manuscript; D.J.M., D.D.P., D.R., A.S.W., O.V.S., and N.-H.H.-R. edited and revised manuscript; D.J.M., D.D.P., D.R., A.S.W., O.V.S., and N.-H.H.-R. approved final version of manuscript.

REFERENCES

1. **Bayram S.** Modeling TGF-mediated flow dynamics in a system of three coupled nephrons. *Int J Numer Methods Biomed Eng* 28: 384–399, 2012. doi:10.1002/cnm.2471.
2. **Bayram S, Stepien TL, Pitman EB.** TGF-mediated dynamics in a system of many coupled nephrons. *Bull Math Biol* 71: 1482–1506, 2009. doi:10.1007/s11538-009-9410-1.
3. **Beeuwkes R 3rd.** Efferent vascular patterns and early vascular-tubular relations in the dog kidney. *Am J Physiol* 221: 1361–1374, 1971.
4. **Beeuwkes R 3rd, Bonventre JV.** Tubular organization and vascular-tubular relations in the dog kidney. *Am J Physiol* 229: 695–713, 1975.
5. **Boas DA, Dunn AK.** Laser speckle contrast imaging in biomedical optics. *J Biomed Opt* 15: 011109, 2010. doi:10.1117/1.3285504.

6. **Casellas D, Carmines PK, Dupont M, Redon P, Moore LC.** Arteriolar renin and vascular effects of angiotensin II in juxtamedullary nephrons. *Kidney Int Suppl* 30: S60–S64, 1990.
7. **Casellas D, Dupont M, Bouriquet N, Moore LC, Artuso A, Mimran A.** Anatomic pairing of afferent arterioles and renin cell distribution in rat kidneys. *Am J Physiol Renal Physiol* 267: F931–F936, 1994.
8. **Cassot F, Lauwers F, Fouard C, Prohaska S, Lauwers-Cances V.** A novel three-dimensional computer-assisted method for a quantitative study of microvascular networks of the human cerebral cortex. *Microcirculation* 13: 1–18, 2006. doi:10.1080/10739680500383407.
9. **Chen YM, Yip KP, Marsh DJ, Holstein-Rathlou NH.** Magnitude of TGF-initiated nephron-nephron interactions is increased in SHR. *Am J Physiol Renal Physiol* 269: F198–F204, 1995.
10. **Chon KH, Raghavan R, Chen YM, Marsh DJ, Yip KP.** Interactions of TGF-dependent and myogenic oscillations in tubular pressure. *Am J Physiol Renal Physiol* 288: F298–F307, 2005. doi:10.1152/ajprenal.00164.2004.
11. **Christensen EI, Grann B, Kristoffersen IB, Skriver E, Thomsen JS, Andreasen A.** Three-dimensional reconstruction of the rat nephron. *Am J Physiol Renal Physiol* 306: F664–F671, 2014. doi:10.1152/ajprenal.00522.2013.
12. **Dunn OJ.** Multiple comparisons using rank sums. *Technometrics* 6: 241–252, 1964. doi:10.1080/00401706.1964.10490181.
13. **Feldberg R, Colding-Jørgensen M, Holstein-Rathlou NH.** Analysis of interaction between TGF and the myogenic response in renal blood flow autoregulation. *Am J Physiol Renal Physiol* 269: F581–F593, 1995.
14. **Garcia-Sanz A, Rodriguez-Barbero A, Bentley MD, Ritman EL, Romero JC.** Three-dimensional microcomputed tomography of renal vasculature in rats. *Hypertension* 31: 440–444, 1998. doi:10.1161/01.HYP.31.1.440.
15. **Holstein-Rathlou NH.** Synchronization of proximal intratubular pressure oscillations: evidence for interaction between nephrons. *Pflügers Arch* 408: 438–443, 1987. doi:10.1007/BF00585066.
16. **Holstein-Rathlou NH, He J, Wagner AJ, Marsh DJ.** Patterns of blood pressure variability in normotensive and hypertensive rats. *Am J Physiol Renal Physiol* 269: R1230–R1239, 1995.
17. **Holstein-Rathlou NH, Leyssac PP.** TGF-mediated oscillations in the proximal intratubular pressure: differences between spontaneously hypertensive rats and Wistar-Kyoto rats. *Acta Physiol Scand* 126: 333–339, 1986. doi:10.1111/j.1748-1716.1986.tb07824.x.
18. **Holstein-Rathlou NH, Sosnovtseva OV, Pavlov AN, Cupples WA, Sorensen CM, Marsh DJ.** Nephron blood flow dynamics measured by laser speckle contrast imaging. *Am J Physiol Renal Physiol* 300: F319–F329, 2011. doi:10.1152/ajprenal.00417.2010.
19. **Holstein-Rathlou NH, Yip KP, Sosnovtseva OV, Mosekilde E.** Synchronization phenomena in nephron-nephron interaction. *Chaos* 11: 417–426, 2001. doi:10.1063/1.1376398.
20. **Horacek MJ, Earle AM, Gilmore JP.** An investigation of potential vascular connections between the kidney and the adrenal gland. *Acta Anat (Basel)* 123: 9–13, 1985. doi:10.1159/000146030.
21. **Horacek MJ, Earle AM, Gilmore JP.** The renal microvasculature of the monkey: an anatomical investigation. *J Anat* 148: 205–231, 1986.
22. **Horacek MJ, Earle AM, Gilmore JP.** The renal vascular system of the monkey: a gross anatomical description. *J Anat* 153: 123–137, 1987.
23. **Jiang ZL, Kassab GS, Fung YC.** Diameter-defined Strahler system and connectivity matrix of the pulmonary arterial tree. *J Appl Physiol (1985)* 76: 882–892, 1994.
24. **Källskog O, Marsh DJ.** TGF-initiated vascular interactions between adjacent nephrons in the rat kidney. *Am J Physiol Renal Physiol* 259: F60–F64, 1990.
25. **Kassab GS, Rider CA, Tang NJ, Fung YC.** Morphometry of pig coronary arterial trees. *Am J Physiol Heart Circ Physiol* 265: H350–H365, 1993.
26. **Kriz W, Bankir L; The Renal Commission of the International Union of Physiological Sciences (IUPS).** A standard nomenclature for structures of the kidney. *Kidney Int* 33: 1–7, 1988. doi:10.1038/ki.1988.1.
27. **Laugesen JL, Sosnovtseva OV, Mosekilde E, Holstein-Rathlou NH, Marsh DJ.** Coupling-induced complexity in nephron models of renal blood flow regulation. *Am J Physiol Regul Integr Comp Physiol* 298: R997–R1006, 2010. doi:10.1152/ajpregu.00714.2009.
28. **Layton AT, Moore LC, Layton HE.** Multistable dynamics mediated by tubuloglomerular feedback in a model of coupled nephrons. *Bull Math Biol* 71: 515–555, 2009. doi:10.1007/s11538-008-9370-x.
29. **Leyssac PP, Holstein-Rathlou NH.** Effects of various transport inhibitors on oscillating TGF pressure responses in the rat. *Pflügers Arch* 407: 285–291, 1986. doi:10.1007/BF00585304.
30. **Marsh DJ, Osborn JL, Cowley AW Jr.** 1/*f* fluctuations in arterial pressure and regulation of renal blood flow in dogs. *Am J Physiol Renal Physiol* 258: F1394–F1400, 1990.
31. **Marsh DJ, Sosnovtseva OV, Chon KH, Holstein-Rathlou NH.** Nonlinear interactions in renal blood flow regulation. *Am J Physiol Regul Integr Comp Physiol* 288: R1143–R1159, 2005. doi:10.1152/ajpregu.00539.2004.
32. **Marsh DJ, Sosnovtseva OV, Mosekilde E, Holstein-Rathlou NH.** Vascular coupling induces synchronization, quasiperiodicity, and chaos in a nephron tree. *Chaos* 17: 015114, 2007. doi:10.1063/1.2404774.
33. **Marsh DJ, Sosnovtseva OV, Pavlov AN, Yip KP, Holstein-Rathlou NH.** Frequency encoding in renal blood flow regulation. *Am J Physiol Regul Integr Comp Physiol* 288: R1160–R1167, 2005. doi:10.1152/ajpregu.00540.2004.
34. **Marsh DJ, Toma I, Sosnovtseva OV, Peti-Peterdi J, Holstein-Rathlou NH.** Electrotonic vascular signal conduction and nephron synchronization. *Am J Physiol Renal Physiol* 296: F751–F761, 2009. doi:10.1152/ajprenal.90669.2008.
35. **Marsh DJ, Wexler AS, Brazhe A, Postnov DE, Sosnovtseva OV, Holstein-Rathlou NH.** Multinephron dynamics on the renal vascular network. *Am J Physiol Renal Physiol* 304: F88–F102, 2013. doi:10.1152/ajprenal.00237.2012.
36. **Marxen M, Sled JG, Henkelman RM.** Volume ordering for analysis and modeling of vascular systems. *Ann Biomed Eng* 37: 542–551, 2009. doi:10.1007/s10439-008-9623-8.
37. **More RH, Duff GL.** The renal arterial vasculature in man. *Am J Pathol* 27: 27–95, 1951.
38. **Murray CD.** The physiological principle of minimum work. I. The vascular system and cost of blood volume. *Proc Natl Acad Sci USA* 12: 207–214, 1926. doi:10.1073/pnas.12.3.207.
39. **Nordsletten DA, Blackett S, Bentley MD, Ritman EL, Smith NP.** Structural morphology of renal vasculature. *Am J Physiol Heart Circ Physiol* 291: H296–H309, 2006. doi:10.1152/ajpheart.00814.2005.
40. **Osipov GV, Kurths J, Zhou C.** *Synchronization in Oscillatory Networks*. Berlin: Springer, 2010.
41. **Pitman EB, Zaritski RM, Kesseler KJ, Moore LC, Layton HE.** Feedback-mediated dynamics in two coupled nephrons. *Bull Math Biol* 66: 1463–1492, 2004. doi:10.1016/j.bulm.2004.01.006.
42. **Postnov DD, Marsh DJ, Postnov DE, Braunstein TH, Holstein-Rathlou NH, Martens EA, Sosnovtseva O.** Modeling of kidney hemodynamics: probability-based topology of an arterial network. *PLOS Comput Biol* 12: e1004922, 2016. doi:10.1371/journal.pcbi.1004922.
43. **Postnov DD, Postnov DE, Marsh DJ, Holstein-Rathlou NH, Sosnovtseva OV.** Dynamics of nephron-vascular network. *Bull Math Biol* 74: 2820–2841, 2012. doi:10.1007/s11538-012-9781-6.
44. **Schröder S, Brab M, Schmid-Schönbein GW, Reim M, Schmid-Schönbein H.** Microvascular network topology of the human retinal vessels. *Fortschr Ophthalmol* 87: 52–58, 1990.
45. **Sosnovtseva OV, Pavlov AN, Mosekilde E, Holstein-Rathlou NH, Marsh DJ.** Double-wavelet approach to studying the modulation properties of nonstationary multimode dynamics. *Physiol Meas* 26: 351–362, 2005. doi:10.1088/0967-3334/26/4/002.
46. **Sosnovtseva OV, Pavlov AN, Mosekilde E, Yip KP, Holstein-Rathlou NH, Marsh DJ.** Synchronization among mechanisms of renal autoregulation is reduced in hypertensive rats. *Am J Physiol Renal Physiol* 293: F1545–F1555, 2007. doi:10.1152/ajprenal.00054.2007.
47. **Strahler A.** Hypsometric (area altitude) analysis of erosional topology. *Bull Geol Soc Am* 63: 1117, 1952. doi:10.1130/0016-7606(1952)63[1117:HAAOET]2.0.CO;2.
48. **Wagner AJ, Holstein-Rathlou NH, Marsh DJ.** Internephron coupling by conducted vasomotor responses in normotensive and spontaneously hypertensive rats. *Am J Physiol Renal Physiol* 272: F372–F379, 1997.
49. **Yip KP, Holstein-Rathlou NH, Marsh DJ.** Dynamics of TGF-initiated nephron-nephron interactions in normotensive rats and SHR. *Am J Physiol Renal Physiol* 262: F980–F988, 1992.
50. **Yip KP, Holstein-Rathlou NH, Marsh DJ.** Mechanisms of temporal variation in single-nephron blood flow in rats. *Am J Physiol Renal Physiol* 264: F427–F434, 1993.